Sensitive Biosensing Using Plasmonic Enhancement of Fluorescence by Rapid Thermal Annealed Silver Nanostructures

Shuangming Li and Venkat R. Bhethanabotla, *Senior Member, IEEE*

***Abstract*—Although immunofluorescence assays have been used for decades, they are not traditionally capable of quantifying biomarkers at ng/ml levels. Plasmonic enhancement of fluorescence using metallic surface nanostructures has exhibited potential in amplifying the fluorescence signal, which could reduce limits of detection and increase sensitivity. However, current methods for fabricating metallic nanostructures, such as e-beam nanolithography, colloidal lithography, and colloidal self-assembly, require complicated processes and have various drawbacks. In this work, we describe a nanostructure fabrication process we have developed based on the dewetting of thin silver films by rapid thermal annealing, which is suitable for large areas. The nanostructures were then coated with a thin silica film to protect them and also to control the distance between the metallic surface and fluorophores, an important parameter when tuning metal enhancement of fluorescence. Antibody-antigen immunoassays utilizing immunoglobulin G were applied to evaluate the fluorescence enhancement from these nanostructures. A nearly 19-fold increase in the fluorescence intensity was achieved with an optimized structure. Calibration of the resulting plasmonically enhanced immunofluorescence sensor showed that it is nearly 13 times more sensitive than the non-enhanced version and was capable of quantification of a biomarker at ∼ 1 ng/ml levels. A model nanostructure was constructed for which finite difference time domain simulations were in good agreement with experimental results, allowing for optimization of process conditions for the further generation of nanostructures.**

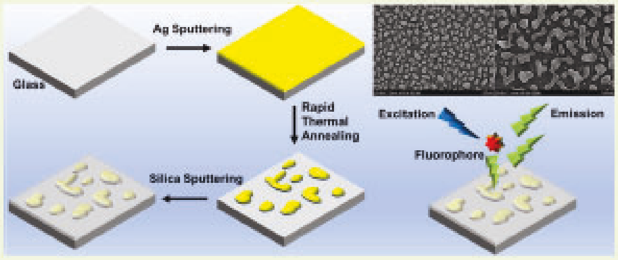

***Index Terms*— Metal-enhanced fluorescence, immunoassays, nanoparticles, rapid thermal annealing, immunofluorescence, nanostructure.**

I. INTRODUCTION

FLUORESCENCE has been used for sensing technology in many areas such as protein, DNA and cell detection [1]. Metallic surfaces can affect fluorescence in various ways – quenching it or increasing rates of excitation or quantum yield [2]. Silver and gold nanostructures, generating surface plasmon resonance in the visible light range, have been widely used in biosensing [3], surface enhanced Raman spectroscopy [4], near-field optics [5], etc.

Nano-scale metallic particles or structures can alter the fluorophores' free-space condition and can result in dramatic spectral changes. Metal surfaces can increase or decrease the radiative decay rates of fluorophores and can increase the extent of resonant energy transfer. The effects of metallic surfaces include three mechanisms: quenching via energy transfer at short distances (~0–5 nm), concentration of the incident light field (~0–15 nm), and increasing the intrinsic radiative decay rate of the fluorophore (~0–20 nm)[6]. The use of fluorophore–metal interactions in biotechnology has primarily been referred to as radiative decay engineering or metal-enhanced fluorescence (MEF)[7]. The free-space quantum yields (Q_0) and the enhanced fluorescence signal's quantum yield (Q_m) of fluorophores in close proximity to metallic nanostructures could be described by the following equations[8]:

$$Q_0 = \Gamma / (\Gamma + k_{nr}) \tag{1}$$

$$Q_m = (\Gamma + \Gamma_m) / (\Gamma + \Gamma_m + k_{nr}) \tag{2}$$

where Γ is the unmodified radiative decay rate and k_{nr} is the non-radiative rate. The presence of a nearby metallic surface increases the radiative rate by the addition of a new rate Γ_m.

Manuscript received March 15, 2021; revised April 21, 2021; accepted April 21, 2021. Date of publication April 26, 2021; date of current version July 14, 2021. This work was supported by the National Science Foundation under Grant IIP-1640668. The associate editor coordinating the review of this article and approving it for publication was Prof. Yu-Cheng Lin. *(Corresponding author: Venkat R. Bhethanabotla.)*

Shuangming Li was with the Department of Chemical and Biomedical Engineering, University of South Florida, Tampa, FL 33620 USA. He is now with Sensel Inc., Sunnyvale, CA 94085 USA (e-mail: shuangming@mail.usf.edu).

Venkat R. Bhethanabotla is with the Department of Chemical and Biomedical Engineering, University of South Florida, Tampa, FL 33620 USA (e-mail: bhethana@usf.edu).

This article has supplementary downloadable material available at https://doi.org/10.1109/JSEN.2021.3075637, provided by the authors.

Digital Object Identifier 10.1109/JSEN.2021.3075637

Several methods to realize the metal-enhanced fluorescence effect on substrates have been reported in the literature. Generally, methods for fabricating nanopatterns on a substrate are not practical, and are unsuitable for large areas required in biosensing applications. Electron-beam lithography is a widely used method to establish nanostructures [9]. It involves metal lift-off or plasma etching and provides high resolution and reproducibility with precise pattern control over geometry down to the nanometer scale. However, in addition to requiring expensive equipment, it is impractical for the fabrication of large areas. Another method is photo or laser–interference lithography [10], [11]. It exposes a photoresist layer to two or more coherent light beams, providing a nanolithographic technique for periodically-patterned structures. This method requires a specially-designed optical system with beam splitters and mirrors to generate multiple light beams. The angles of incidence can be varied by changing the distances between mirrors or between sample plane and mirror plane. When the beams reach the sample surface, optical interference results in various interference patterns. Although providing a rapid and larger-area nanolithography process, it still requires a complicated optical system and a precise – and therefore, expensive – alignment platform [12]. Nanoimprint lithography is another method of fabricating nanometer-scale patterns on a large scale [13]. A mold is first fabricated using conventional electron-beam lithography. The mold patterns are transferred to the photoresist layer on the sample substrate via the UV and imprint processes. However, this method typically requires fabrication of a precise nanopattern mold and release layer in addition to a special imprinting system. Some self-masked methods such as polystyrene beads [14] or colloidal lithography [15] have also been reported. These methods use small particles such as polystyrene beads or metal particle coatings on the substrate. Coating patterns with the area covered and uncovered work as masks for lithography processes such as metal deposition and dry etching. This method requires no complicated lithographic processes or lengthy fabrication times. However, the pattern quality and shape are highly dependent on the assembly area density and space between each particle. There are also some methods that eschew lithography such as electrochemical growth [16] or nanoparticle assembly [7], [17]. Using colloid chemistry, metal nanoparticles with various structures such as triangular prisms, cubes, rods, and wires can be synthesized [18]. This allows for investigation of the effects of nanoparticle size, composition, and self-assembly – however, uniform distribution of these particles on the surface is a problem, as is ensuring their stability during sensor usage.

In previous publications [19], [20], we have reported on the effects of nanoparticle structure and compositions on MEF. In a recent publication [21], we have applied MEF from colloidally-synthesized silver nanocubes dispersed on a substrate to construct a biosensor for the cancer marker carcinoembryonic antigen (CEA) to demonstrate quantification in the low ng/ml levels. The quantum yield enhancement is dependent on the nanocube dimension, areal density, and distance between fluorophores and the particle surface. Though successful at lowering the detection limit and allowing for detection in a surface acoustic wave sensor platform, the silver-nanocube-based MEF immunofluorescence assay has several drawbacks. Notable among them are the unreliable colloidal synthesis procedure and its scale-up, difficult-to-achieve uniform distribution of the nanocubes on the surface at the specified areal density, and difficulty with adhesion of these cubes to the surface throughout the sensing process. The colloidal synthesis and assembly of nanoparticles is extremely sensitive to many factors such as reaction time, temperature control, and surface modification. The adhesion of particles to a sensor surface while retaining MEF and without affecting sensor performance is not easily achieved. Both of these factors preclude the use of nanoparticles produced by colloidal synthesis in MEF-based biosensor applications. To overcome these issues and attain faster and easier nanostructure fabrication, we have implemented a rapid thermal annealing (RTA) process to obtain stable nanostructures. Upon optimization, and after coating with a silica overlayer, we were able to achieve a stable nanostructure that showed exceptionally high MEF, allowing for the construction of a robust, sensitive, and low-limit-of-detection biosensor suitable for cancer biomarker quantification.

RTA is typically used for improving structures via intrinsic stress liberation and controlling surface roughness [22]. Metallic thin films deposited on dielectric substrates are typically thermodynamically unstable or sub-stable. The spreading coefficient S determines if the liquid spontaneously spreads ($S > 0$) or coagulates ($S < 0$), with S defined as [23]:

$$S = \gamma_{sg} - \gamma_{lg} - \gamma_{ls} \tag{3}$$

The interfacial tensions of solid-gas (γ_{sg}), liquid-gas (γ_{lg}), and liquid-solid (γ_{ls}) interfaces, represent the surface energy between each of these interfaces. Spontaneous dewetting of metallic thin films on a dielectric substrate to form nanoparticles has been studied and can be achieved via thermal annealing [24], laser treatment [25], [26], ion bombardment [27], etc.. The complex mechanisms involved in forming the nanostructures have been investigated via molecular dynamics and continuum approaches, however, the different length and time scales involved makes it difficult to predict the nonlinear dewetting dynamics needed to quantitatively assess film-thickness-dependent nanostructure characteristics [28]. Difficulty in process modeling and control is a key shortcoming in the production of nanostructures via spontaneous dewetting of thin films, and failure to control this variable leads to nonuniformity in particle size and structure and to defects in general. Fortunately, MEF is largely tolerant to such imperfections. In this work, we have utilized RTA to perturb the film into discontinuous droplets of flat island shapes to reach a new equilibrium structure that minimizes the interfacial energy. When the metallic film is very thin, this process can occur at a temperature much lower than its melting point. After the RTA process, disordered nano-islands are formed, allowing for the fabrication of larger-area nanostructures on the substrate. The value of such micron-sized island structures in the plasmonic enhancement of fluorescence of fluorophore-conjugated antibodies during immunosensing is the subject of this contribution. Additionally, we find that these RTA-treated nanoislands are not strongly attached to the substrate. Hence, we have coated them with a thin layer of silicon dioxide, to not only help stabilize the nanostructures, but also to protect the silver from oxidizing during sensor storage and operation. The effect of this dielectric film and its properties (such as thickness) on MEF is described in this work. The RTA process is optimized to produce a large plasmonic enhancement of the fluorescent intensity in antibody-antigen immunoassays using immunoglobulins (IgGs). Optimized devices have shown significantly larger sensitivities, and limits of detection on the ng/ml levels were achieved in these assays. Results of this work point to the possibility of achieving point-of-need quantification of biomarkers via immunofluorescence.

II. MODELS AND SIMULATIONS

Experiential research exists on the fluorescent enhancement of metallic nanoparticles and dielectric layers [29], however the mechanism by which the dimensions of the nanoparticle and dielectric layer influence the effect has not been fully ascertained. The finite difference time-domain (FDTD) simulation is widely used in computational electrodynamics. We utilized FDTD simulations to predict fluorescent enhancement for a model system suitable for exploring the relationship between fluorescent enhancement and nanoparticle geometry with the long-term aim of improving device design. A fluorophore was localized above the nanoparticle as schematically illustrated in Figure 1a, in which the annealed silver particle is idealized as a circular disk of radius (R), thickness (T), and silica coating layer height (H), and the fluorophore is considered to be a dipole located at a distance D from the particle surface. Figure 1b demonstrates that the enhancement factor is dependent on the distance between the particle surface and the fluorophore. The simulation script can be found in Supplemental Materials.

Calculations were performed for nanoparticles without silica coatings (H = 0 nm) for particles of thickness T equal to 50 nm, 25 nm, and 15 nm. The particle radius R selected for each thickness was based on the results of the experimental size distribution, with average particle radius being 200 nm, 50 nm, and 20 nm, respectively. Figure 2 shows that the thickest nanoparticle (T = 50 nm) enhances fluorescence the most, compared to the other two cases, whose enhancement factors are less than 2. The silica coating layer also has an effect on the spectrum. Increasing silica thickness (H) red-shifts the spectrum peak from 464 nm to 503 nm. For the typical fluorophore such as Alexa 488, the emission peak is at 520 nm, for which the 15 nm silica layer shows an enhancement factor to 7.01 compared to 4.42 for silica thickness of 0 nm. These simulations provide guidance for the optimal selection of nanoparticle sizes and silica layer thicknesses for a given fluorescence dye.

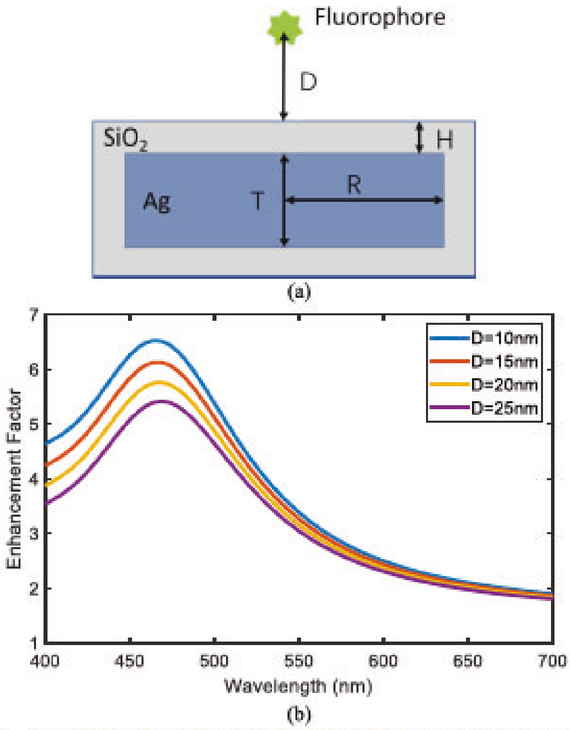

Fig. 1. (a) Schematic of the FDTD computational model; (b) computed fluorescence enhancement factor as a function of distance between the fluorophore and silver particle surface. In this simulation, T = 50 nm, R = 200 nm, H = 0 nm, and D = 10 to 25 nm.

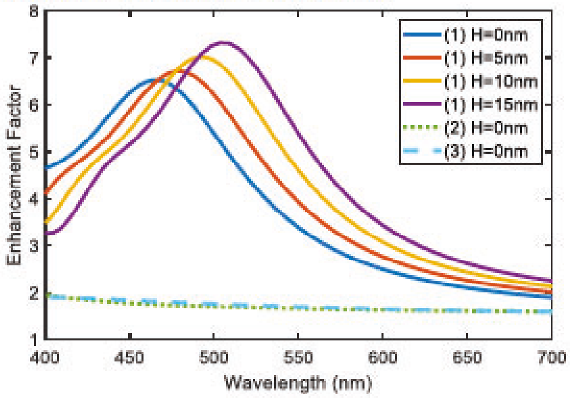

Fig. 2. Computed fluorescence enhancement factor for several SiO_2 coating thicknesses. In these simulations, (1) solid lines are for: T = 50 nm, R = 200 nm, D = 10 nm, and H = 0 nm to 15 nm; (2) dotted lines are for: T = 15 nm, R = 20 nm, D = 10 nm, and H = 0 nm; and (3) dashed lines are for: T = 25 nm, R = 50 nm, D = 10 nm, and H = 0 nm.

III. EXPERIMENTAL

A. Reagents and Apparatus

All materials and reagents were of analytical grade and were used as received. Rabbit IgG, bovine serum albumin (BSA), and (3-aminopropyl) - triethoxysilane (APTES) were purchased from Sigma-Aldrich. Mouse anti-rabbit IgG-CFL 488 was purchased from Santa Cruz Biotechnology. Protein A was purchased from Abcam. Reagent grade deionized water (DI water) with 18.2 MΩ·cm resistivity was produced in the laboratory using a Millipore system.

The instruments utilized in the experiments were a Hitachi SU-70 Scanning Electron Microscope (SEM), a Nikon FN1 fluorescence microscope, an MTI rapid thermal processor, and a Jasco V-670 spectrophotometer.

B. Chip Fabrication

The chip fabrication process is illustrated in Figure 3. The glass slides were cleaned using a piranha solution (concentrated sulfuric acid: 30% hydrogen peroxide solution

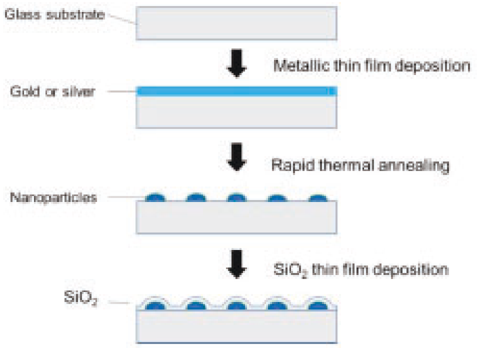

Fig. 3. Schematic illustration of fabrication process for metallic nanostructures with silica coating layer on a SiO_2 glass substrate.

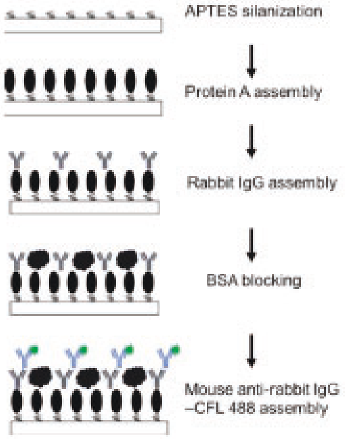

Fig. 4. Schematic diagram of chip modification processes for fluorescence immunoassays.

in ratio of 3:1). After cleaning, a thin metal (gold or silver) film was deposited on the slides. E-beam evaporation and sputtering were both used to evaluate the deposition quality. A deposition rate of 2.5 Å/s was found to be the maximum that could produce a homogeneous film. In one optimized test, the slides were treated by a RTA process in which they were rapidly heated up to 500°C at a rate of 25 °C/s and held there for 60 seconds. Then, the slides were cooled to room temperature gradually. The entire process was conducted in a N_2 gas atmosphere in an MTI rapid thermal processor. The nanostructured patterns were generated after this annealing treatment. A thin SiO_2 layer was sputtered on the annealed slide surface with a deposition rate of 4 Å/min. The fabricated slides were diced into individual chips for further tests.

C. Chips Modification

The fabricated slides were modified with biomolecules using the following processes. The slides were first solvent rinsed and dried with N_2 gas. Ten mM APTES in pure ethyl alcohol solution was used to silanize the slide surface. After 1 hour of soaking, the chips were washed with pure ethyl alcohol and dried with N_2 gas. The biomolecular surface assembly strategy is shown schematically in Figure 4. The silanized surface was incubated with 200 μg/ml Protein A at in PBS for 2 hours at room temperature. The partly-functionalized surface was the incubated with Rabbit IgG for 2 hours followed by 1 mg/ml BSA in PBS for blocking the unbound sites on the substrate. Later, 4 μg/ml mouse anti rabbit IgG-CFL 488 was used as the detection antibody during fluorescence testing. The IgG conjugate Cruz Fluor^{TM} 488 has an excitation peak of 491 nm and an emission peak of 520 nm. The chips were rinsed with PBS and dried with N_2 gas between each step.

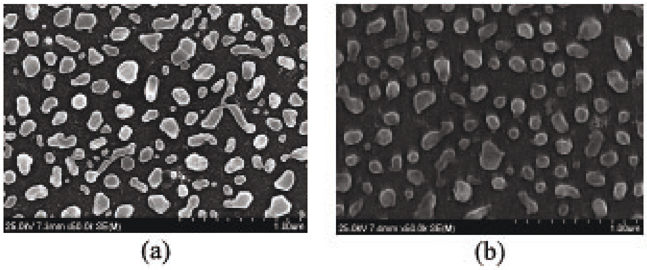
(a) (b)

Fig. 5. SEM images of the annealed 125 Å film: (a) gold; (b) silver. The metallic layers were deposited using e-beam evaporation. Scale bar is 1 micron.

IV. RESULTS AND DISCUSSIONS

A. Comparison of Gold and Silver Nanostructures

To understand the RTA process and fluorescence enhancement better, we deposited gold and silver on the glass slides with the same deposition and thermal annealing processes. The film thickness was 125 Å. Figure 5 shows SEM images of the gold and silver nanoparticles. No significant differences in distribution are apparent between the 2 metals.

A Nikon FN1 fluorescence microscope was used to measure the fluorescent intensity. The microscope light intensity was set to 100% of the solar light source with an exposure time of 10 seconds and a gain of 1 X. The solar light was filtered through a blue light filter as the excitation light. The emission light was filtered through a green light filter as the detection signal. The fluorescence images were collected and the green channel values of the RGB system (255,255,255) were calculated. The fluorescence results clearly show that the gold nanoparticles quench, and silver particles enhance fluorescent intensity compared to an ordinary glass slide was treated using the same functionalization process. This quenching from gold nanoparticles is expected and is a result of the non-radiative energy transfer from the excited states of the fluorophores to the gold particles [30], [31]. As shown in Figure 6, the presence of silver nanoparticles significantly increased the fluorescent intensity almost up to the limit of detection of 255.

B. Silver Nanoparticles From e-Beam and Sputter Deposited Films

The silver thin films were deposited using e-beam evaporation and sputtering for deposition process comparison. The resulting nanostructures were compared using SEM and fluorescence microscopy. SEM images of the annealed nanopatterns from these two methods show no visible difference, but as shown in Figure 7a, however, soaking and washing multiple times during the surface modification processes, the

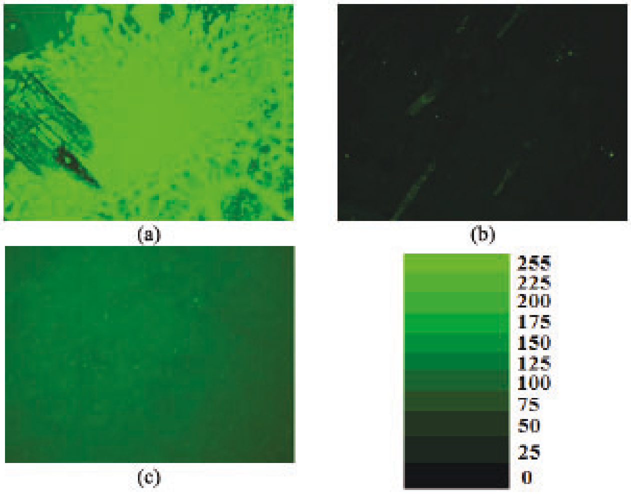

Fig. 6. Fluorescence intensity enhancement from (a) silver nanoparticles; (b) gold nanoparticles; compared to that from (c) bare glass. The metallic layers were deposited using e-beam evaporation and light source dose was set to 100%.

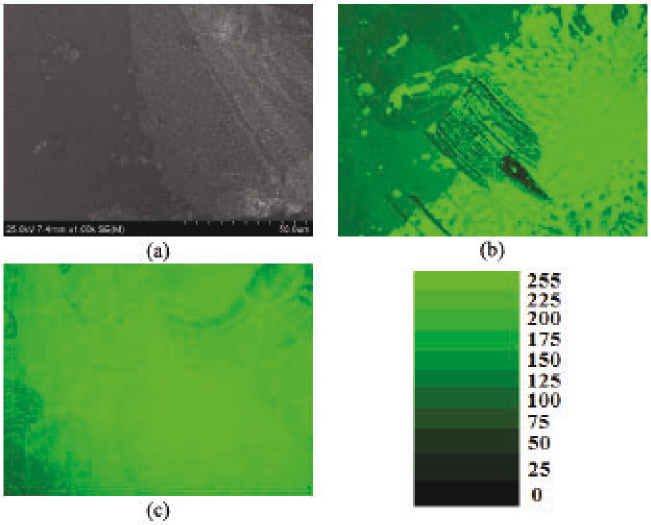

Fig. 7. (a) SEM image of silver nanopatterns via e-beam evaporation after rising process. (b) Fluorescence image of silver nanopatterns via e-beam evaporation and (c) sputter deposition.

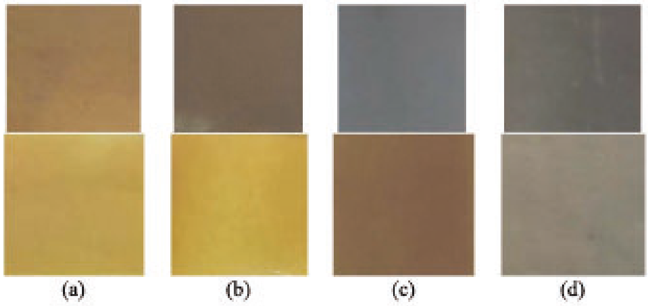

Fig. 8. Photographs of glass slides before (top row) and after (bottom row) the RTA process for sputter deposited films of thickness: (a) 5 nm; (b) 10 nm; (c) 15 nm; (d) 25nm.

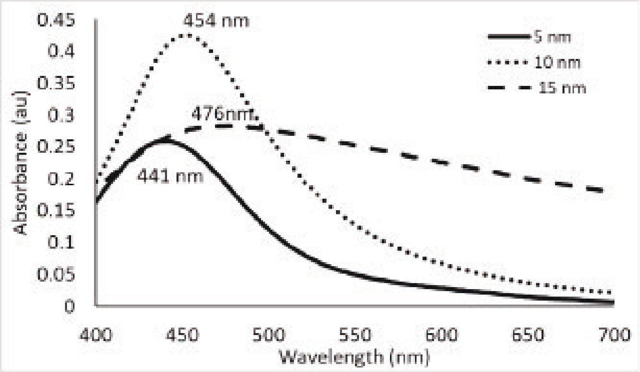

Fig. 9. UV-vis absorbance spectra of RTA treated silver nanopatterns of deposition thickness 5 nm, 10nm, and 15 nm.

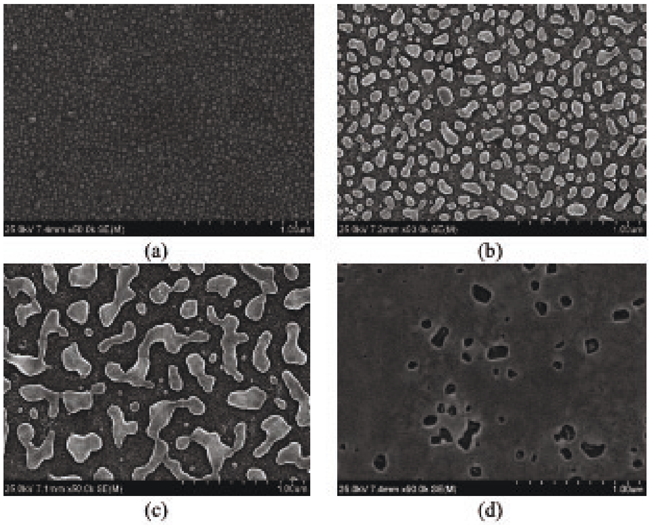

Fig. 10. SEM images of annealed silver films deposited using sputtering: (a) 5 nm; (b) 10 nm; (c) 15 nm; (d) 25 nm. Scale bar is 1 micron.

e-beam samples showed poorer adhesion to the surface. The area where the nanopatterns are absent exhibits much weaker fluorescence intensity as shown in Figure 7b. The sputtered silver sample has better adhesion with the glass surface (Figure 7c), hence, sputtering was utilized as the deposition method in the rest of this study.

C. Silver Nanopattern Characteristics

RTA could significantly change the surface characteristics of the silver film. The images in Figure 8 show the color change after annealing. The 5 nm, 10 nm, 15 nm, and 25 nm films were different colors due to differences in light scattering and absorption [32], [33]. The annealed nanoparticle sizes are highly correlated to the film thicknesses. Thicker layers can generate larger particles and have absorption spectra with broader peaks at longer wavelengths [34]. However, if the silver layer was over-deposited (thicker than 25 nm), the film lost the ability to transform into nanostructures, which shows a mirror effect rather than a surface plasmon effect. As seen from the UV-vis absorbance peaks in Figure 9, the wavelength of the absorbance peak red shifts from 441 nm to 476 nm and becomes wider with increase in the deposited film thickness.

As shown in Figure 10a-c, the thin silver film can produce isolated nanoislands on the glass surface. The 5 nm silver layer

TABLE I
NANOPARTICLE CHARACTERISTICS FOR DIFFERENT DEPOSITED FILM THICKNESS

Film thickness (nm)	5	10	15
Cover area percent (%)	29.8	32.2	31.4
Area density ($/\mu m^2$)	580	66	5.9
Average height (nm)	16.8	31.0	47.5

created hemi-spherical nanopatterns, densely spreading across the entire glass slide. For larger thicknesses, the nanopatterns changed into ellipsoidal or peanut-shaped structures. When the thickness reached 15 nm, worm or lace-like patterns appeared. The pattern lost its isolation when the thickness got up to 25 nm, resulting in a flat film layer without nanostructures (Figure 10d).

D. Silver Nanoparticles Density and Distribution

The particles size, area density and distribution of the 5 nm, 10 nm and 15 nm silver samples were calculated and are shown in Table I. Because the thermal annealing cannot generate regular nanostructures such as spheres and cubes, we calculated area size to analyze the particle distribution. The particle density decreases with increasing film thickness. The annealing treatment created nanopatterns having areas coated and uncoated by silver. However, the ratio of the covered area (~30%) does not change significantly. Since the total volume of the deposited silver is constant, the average height of the annealed nanopattens can be calculated as:

$$Average\ height = \frac{Film\ thickness}{Covered\ area\ fraction} \tag{4}$$

The nanoparticle area distributions are shown in Figure 11. About 39% of the particles from 5 nm annealed film have areas in the range of range 250 - 450 nm^2 which is equal to 18 - 24 nm diameter if considered as spherical in shape. 47% of the particles from 15 nm film have areas in the range of 0.025 – 0.045 μm^2, 100 times larger than those of 5 nm film. From these histograms, we conclude that the particle size increases with film thickness. It is obvious that thinner film can provide better monodispersity with a narrower distribution.

E. Fluorescence Enhancement From Ag Nanostructures

RTA-annealed silver nanopatterns formed from 5 nm, 10 nm, 15 nm, and 25 nm thick films were tested for fluorescent immunoassay detection and compared with tests on nonfunctionalized glass surfaces. The fluorescent intensities of each sample were measured under 4% and 100% of maximum light source intensity. The results indicate that the 10 nm and 15 nm silver samples have large fluorescent enhancements. Results are summarized in Figure 12. Specifically, the nonfunctionalized samples showed fluorescent intensities of 5.62 (4% source intensity) and 76.15 (100% source intensity) of 255 units maximum. Illuminated by a 4%-intensity light source, the 10 nm and 15 nm nanostructures increased the fluorescent intensity by factors of 1.72 and 2.76, respectively. Illuminated by a 100%-intensity light source, these enhancement factors were 1.46 and 2.10, respectively. The 5 nm silver nanostructures had smaller enhancement factors of only about 1.29~1.40 fold. This indicates that the quantum yield enhancement factor is strongly dependent on the nanoparticle dimensions. The 25 nm film resulted in a fluorescence decrease, because the thick film cannot generate the nanostructures, indicating that the flat silver film has no MEF effect. Thus, the 10 nm and 15 nm film samples were selected for the next step, in which SiO_2 was deposited on these particles.

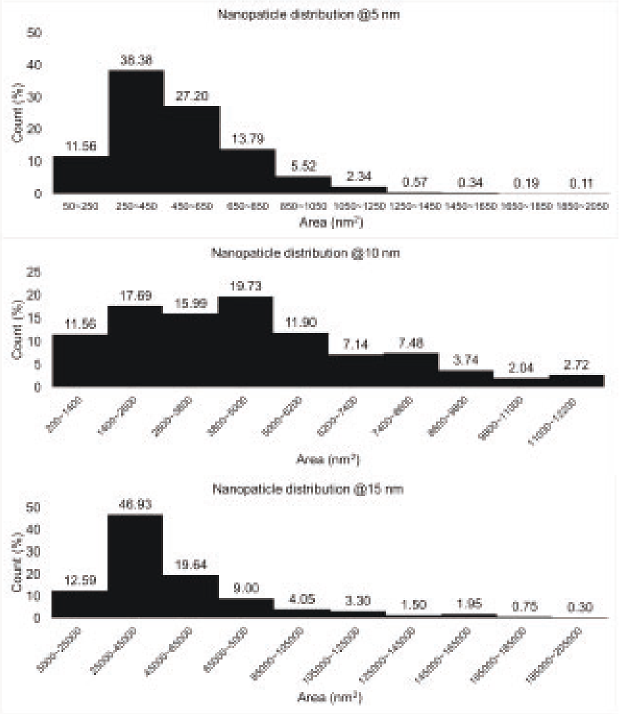

Fig. 11. Area distributions of the RTA treated silver nanostructures for deposition thicknesses of 5nm, 10nm, and 15 nm.

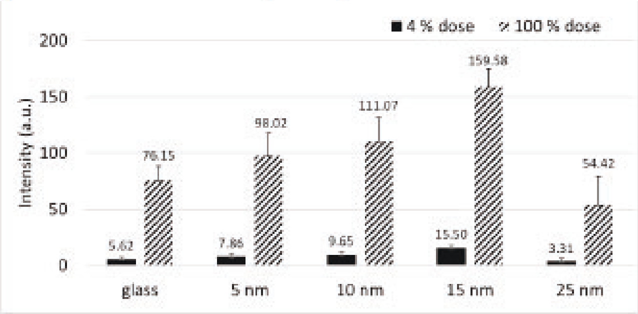

Fig. 12. Enhancement of fluorescent intensity from silver nanoparticles at deposition thicknesses of 5 nm, 10 nm, 15 nm, and 25 nm compared to that of a nonfunctionalized glass slide.

F. Silica Coated Nanostructures

FDTD simulations of the model structures indicate that a silica layer red shifts the plasmonic absorption peak closer to the emission wavelength of the fluorophore, and that the enhancement factors are dependent on the fluorophore-nanoparticle

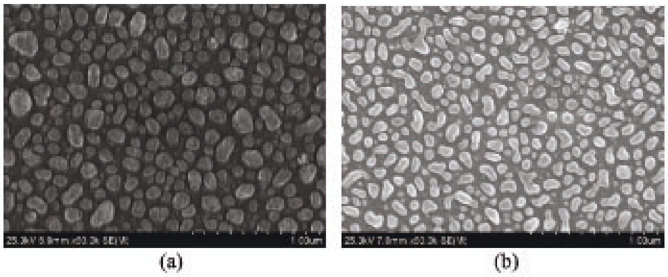

Fig. 13. SEM images of silver nanoparticles after SiO_2 deposition of thicknesses of (a) 5 nm and (b) 10 nm. These particles were generated from the 10 nm silver film. Scale bar is 1 micron.

distance. While the sputter-deposition-generated structures adhere to the substrate better than those generated by e-beam deposition, the silica overlayer stabilizes the nanostructures throughout the sensing process. For these reasons, we investigated the effect of a silica overlayer on MEF for the structures generated from the 10 nm and 15 nm films. Deposition thicknesses of 5 nm and 10 nm were utilized. Figure 13 shows that the nanopatterns are retained after SiO_2 sputtering.

G. MEF From Silica Coated Nanostructures

Four chips with silica-coated nanostructures were utilized in fluorescence immunoassays: a 10 nm silver RTA-treated chip with a 5 nm SiO_2 layer (10 nm Ag @ 5 nm SiO_2), a 10 nm silver RTA-treated chip with a 10 nm SiO_2 layer (10 nm Ag @ 10 nm SiO_2), a 15 nm silver RTA-treated chip with a 5 nm SiO_2 layer (15 nm Ag @ 5 nm SiO_2), and a 15 nm silver RTA-treated chip with a 10 nm SiO_2 layer (15 nm Ag @ 10 nm SiO_2). We found that the samples were overexposed under 100% intensity during fluorescence measurement, which means the SiO_2 layer increases the fluorescent intensity significantly. Thus, the light source intensity was set to 4% for all reported measurements.

The fluorescence images of the glass surface sample and these four samples are shown in Figure 14a-e. All four silica-coated nanostructures show larger fluorescent enhancement compared to the nonfunctionalized glass slide without any nanopatterns, and to the Ag structures without the silica coating. Comparisons of intensities at 4% light source intensity from Figure 12 and 14f show that the SiO_2 coating provides additional enhancement factors of 2.53 for the 10 nm Ag @ 5 nm SiO_2, 4.21 for the 15 nm Ag @ 5 nm SiO_2, 6.19 for the 10 nm Ag @ 10 nm SiO_2, and 6.82 for the 15 nm Ag @ 10 nm SiO_2.

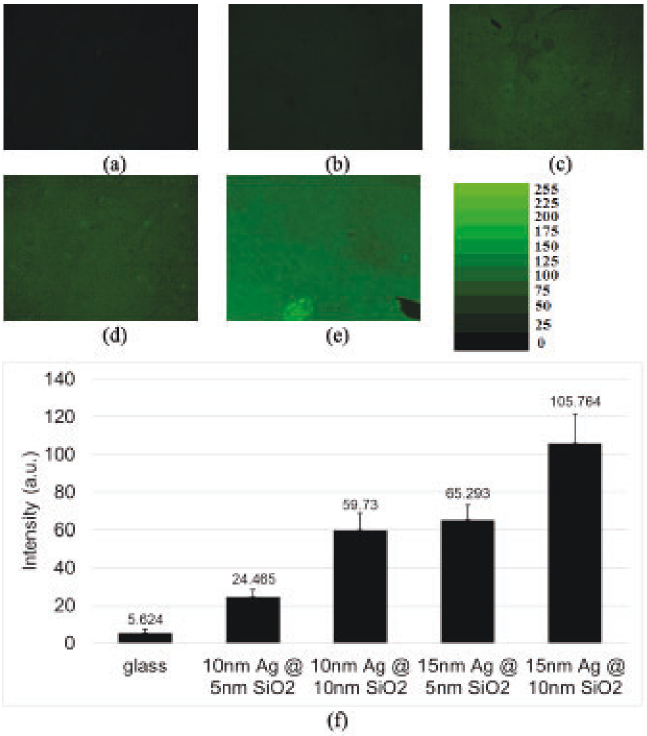

Fig. 14. Fluorescence images of (a) glass slide; (b) 10 nm Ag @ 5 nm SiO_2; (c) 10 nm Ag @ 10 nm SiO_2; (d) 15 nm Ag @ 5 nm SiO_2; (e) 15 nm Ag @ 10 nm SiO_2 and (f) histograms of fluorescence intensity from these samples. The light source intensity was set to 4% of maximum.

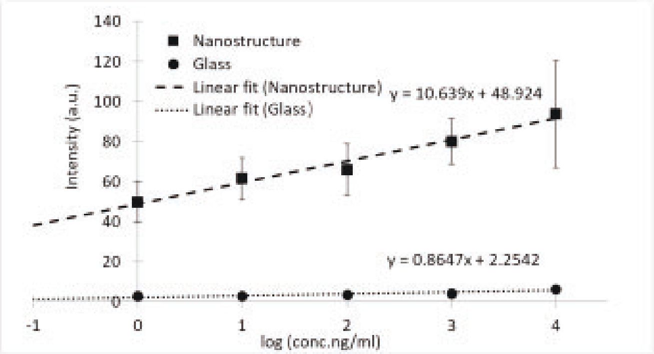

Fig. 15. Calibration curves of the nonfunctionalized and 15 nm Ag @ 10 nm SiO_2 nanostructured sensors.

It would appear that precise control of the distance between the fluorophore and silver nanoparticles is capable of improving enhancement factors in addition to the effect of the dielectric coating on plasmonic phenomena. Each modification layer on the glass chip is a well-established self-assembly monolayer. The APTES film would be of about 7 Å per monolayer [35], [36], however, the APTES film is usually multilayered and is of 2-5 nm thickness in realistic modifications which depend upon surface modification protocols [37], [38]. Protein A of a 42 kDa molecule weight has a rough diameter of 4-5 nm [39]. IgG has a special Y shape with a height of 8.5 nm and cross sectional size/diameter of 20-40 nm [40]–[43]. The average distance from the silver surface to the fluorophore is therefore about 20 - 30 nm including the ~10 nm from the added SiO_2 layer. In addition, the SiO_2 coating introduces a red shift to the plasmonic peak to near the emission peak of the fluorophore, thus increasing the enhancement factor. For this particular immunofluorescence assay, the 15 nm Ag @10 nm SiO_2 samples achieved the maximum enhancement factor of 18.81 in comparison to the nonfunctionalized sample. These results indicate the potential for additional optimization and improved immunoassays.

Sensor calibration curves for a nonfunctionalized glass slide and the 15 nm Ag @ 10 nm SiO_2 sample were constructed and are shown in Figure 15. Fluorescent intensity is linear with the

TABLE II
COMPARISON OF DIFFERENT MEF STRATEGIES

Method	Complexity	Large-scale fabrication	Enhancement factor
This work, RTA-Silica	Easy	Yes	18.81
SiO2-coated silver colloid[44]	Complicated	Yes	10
Surface-deposited silver nanoparticles[45]	Medium	Yes	1.5- 3
Electron beam lithography[46]	Complicated	No	21 -36

logarithm of concentration (ng/ml) over the range of 1−10,000 ng/ml. The sensitivity of the sensor with nanostructures is calculated to be over 12.3 times greater than without due to MEF. These results are encouraging and indicate that the nanostructure MEF device has the potential of achieving sub ng/ml limits of detection in realistic cancer biomarker assays.

Given the easy, fast, and inexpensive fabrication process, the MEF-capable metallic nanostructures with a silica coating layer is a competitive way of improving immunofluorescence assays. A comparison of the enhancement provided by alternate MEF strategies from literature is given in Table II. These strategies are also classified by the complexity in processing and scaling. It is apparent that our proposed method is straightforward, scalable, and capable of achieving one of the highest enhancement factors upon optimization. Although the comparison in Table II is useful and brings out certain helpful features, true comparisons should be made on the basis of actual biosensors and their performances such as presented in this work. For example, the electron beam lithographic technique shows slightly larger enhancement factors than our technique, however, it applies for ordered gold nanostructures coupled to CDS/ZNS nanocrystals dispersed as a polymer blend. Such a system is useful in lighting applications, but not for biosensing, which necessitates the use of fluorophore-conjugated antibodies and overlap of the LSPR peak with the emission frequency. Indeed, we have realized substantial enhancement factors with polymer-dispersed systems using Ag/Cu nanoparticles and ALEXA fluorophores in previously reported studies [19], [20]. It should also be recognized that MEF must translate to lowered LODs and higher sensitivities for biosensor applications as demonstrated in this work.

V. CONCLUSION

In this contribution, a fabrication method to achieve large-area nanostructures using RTA and silica deposition has been described for use in MEF of immunoassays. This method overcomes the drawbacks of other nanostructure fabrication processes such as lithography-based, non-scalable, and other, more complicated processes. A rational process for optimizing the MEF is described based on FDTD calculations and physical reasoning. By optimizing the fluorophore-nanoparticle structure and the red shift of the plasmonic absorption peak using a SiO_2 overlayer, the fluorescent intensity was enhanced by a factor of 18.81 in a typical immunoassay using IgGs. These results provide a great potential for applying MEF in practical biosensing applications.

ABBREVIATIONS

MEF, metal-enhanced fluorescence; RTA, rapid thermal annealing; SEM, scanning electron microscopy; FDTD, finite different time-domain; IgG, immunoglobulin G; BSA, bovine serum albumin; APTES, (3-aminopropyl) – triethoxy-silane.

NOTES

The authors declare the following competing financial interests: A patent has been filed on results related to this research. VRB has financial interest in SenserTec, which develops the technology described in this manuscript.

REFERENCES

[1] A. P. Demchenko, *Introduction to Fluorescence Sensing*. Berlin, Germany: Springer, 2008.

[2] K. Aslan, I. Gryczynski, J. Malicka, E. Matveeva, J. R. Lakowicz, and C. D. Geddes, "Metal-enhanced fluorescence: An emerging tool in biotechnology," *Current Opinion Biotechnol.*, vol. 16, no. 1, pp. 55–62, Feb. 2005.

[3] J. N. Anker, W. P. Hall, O. Lyandres, N. C. Shah, J. Zhao, and R. P. Van Duyne, "Biosensing with plasmonic nanosensors," in *Nanoscience And Technology: A Collection of Reviews From Nature Journals*. Singapore: World Scientific, 2010, pp. 308–319.

[4] T. Vo-Dinh, "Surface-enhanced Raman spectroscopy using metallic nanostructures," *TrAC Trends Anal. Chem.*, vol. 17, nos. 8–9, pp. 557–582, Aug. 1998.

[5] X. Zhang and Z. Liu, "Superlenses to overcome the diffraction limit," *Nature Mater.*, vol. 7, no. 6, pp. 435–441, Jun. 2008.

[6] C. D. Geddes and J. R. Lakowicz, "Metal-enhanced fluorescence," *J. Fluorescence*, vol. 12, pp. 121–129, Aug. 2002.

[7] C. D. Geddes, H. Cao, I. Gryczynski, Z. Gryczynski, J. Fang, and J. R. Lakowicz, "Metal-enhanced fluorescence (MEF) due to silver colloids on a planar surface: Potential applications of indocyanine green to *in vivo* imaging," *J. Phys. Chem. A*, vol. 107, no. 18, pp. 3443–3449, May 2003.

[8] J. R. Lakowicz *et al.*, "Radiative decay engineering: 2. Effects of silver island films on fluorescence intensity, lifetimes, and resonance energy transfer," *Anal. Biochem.*, vol. 301, pp. 261–277, 2002.

[9] W. Yue *et al.*, "Electron-beam lithography of gold nanostructures for surface-enhanced Raman scattering," *J. Micromech. Microeng.*, vol. 22, no. 12, Dec. 2012, Art. no. 125007.

[10] J.-H. Seo *et al.*, "Nanopatterning by laser interference lithography: Applications to optical devices," *J. Nanoscience Nanotechnol.*, vol. 14, no. 2, pp. 1521–1532, Feb. 2014.

[11] Y. Zabila, M. Perzanowski, A. Dobrowolska, M. Kac, A. Polit, and M. Marszalek, "Direct laser interference patterning: Theory and application," *Acta Phys. Polonica-Series A, Gen. Phys.*, vol. 115, pp. 591–593, 2009.

[12] G. S. Pati *et al.*, "Generalized scanning beam interference lithography system for patterning gratings with variable period progressions," *J. Vac. Sci. Technol. B, Microelectron. Nanometer Struct.*, vol. 20, no. 6, p. 2617, 2002.

[13] D. J. Resnick, S. V. Sreenivasan, and C. G. Willson, "Step & flash imprint lithography," *Mater. Today*, vol. 8, no. 2, pp. 34–42, Feb. 2005.

[14] M. Toma, G. Loget, and R. M. Corn, "Fabrication of broadband antireflective plasmonic gold nanocone arrays on flexible polymer films," *Nano Lett.*, vol. 13, no. 12, pp. 6164–6169, Dec. 2013.

[15] Y. Yu and G. Zhang, "Colloidal Lithography," in *Updates in Advanced Lithography*. London, U.K.: InTech, 2013.

[16] Y. Li and G. Shi, "Electrochemical growth of two-dimensional gold nanostructures on a thin polypyrrole film modified ITO electrode," *J. Phys. Chem. B*, vol. 109, no. 50, pp. 23787–23793, Dec. 2005.

[17] J. Liu, S. Li, and V. R. Bhethanabotla, "Metal-enhanced immunofluorescence assays for detection of carcinoembryonic antigen," in *Proc. Conf. SENSORS*, 2017, pp. 1–3.

[18] J. Zhang, M. R. Langille, and C. A. Mirkin, "Photomediated synthesis of silver triangular bipyramids and prisms: The effect of pH and BSPP," *J. Amer. Chem. Soc.*, vol. 132, no. 35, pp. 12502–12510, Sep. 2010.

[19] S. Chowdhury, V. R. Bhethanabotla, and R. Sen, "Effect of Ag-Cu alloy nanoparticle composition on luminescence enhancement/quenching," *J. Phys. Chem. C*, vol. 113, no. 30, pp. 13016–13022, Jul. 2009.

[20] S. Chowdhury, V. R. Bhethanabotla, and R. Sen, "Silver-copper alloy nanoparticles for metal enhanced luminescence," *Appl. Phys. Lett.*, vol. 95, no. 13, Sep. 2009, Art. no. 131115.

[21] J. Liu, S. Li, and V. R. Bhethanabotla, "Integrating metal-enhanced fluorescence and surface acoustic waves for sensitive and rapid quantification of cancer biomarkers from real matrices," *ACS Sensors*, vol. 3, no. 1, pp. 222–229, Jan. 2018.

[22] G. M. Alonzo-Medina, A. González-González, J. L. Sacedón, and A. I. Oliva, "Understanding the thermal annealing process on metallic thin films," *IOP Conf. Series, Mater. Sci. Eng.*, vol. 4, Apr. 2013, Art. no. 012013.

[23] D. J. Srolovitz and M. G. Goldiner, "The thermodynamics and kinetics of film agglomeration," *JOM*, vol. 47, no. 3, pp. 31–36, Mar. 1995.

[24] F. Ruffino and M. G. Grimaldi, "Controlled dewetting as fabrication and patterning strategy for metal nanostructures," *Phys. Status Solidi*, vol. 212, no. 8, pp. 1662–1684, Aug. 2015.

[25] S. Herminghaus *et al.*, "Spinodal dewetting in liquid crystal and liquid metal films," *Science*, vol. 282, p. 916, Oct. 1998.

[26] S. Yadavali, M. Khenner, and R. Kalyanaraman, "Pulsed laser dewetting of au films: Experiments and modeling of nanoscale behavior," *J. Mater. Res.*, vol. 28, no. 13, pp. 1715–1723, Jul. 2013.

[27] X. Hu, D. G. Cahill, and R. S. Averback, "Nanoscale pattern formation in pt thin films due to ion-beam-induced dewetting," *Appl. Phys. Lett.*, vol. 76, no. 22, pp. 3215–3217, May 2000.

[28] C. V. Thompson, "Solid-state dewetting of thin films," *Annu. Rev. Mater. Res.*, vol. 42, no. 1, pp. 399–434, Aug. 2012.

[29] H. Szmacinski, R. Badugu, and J. R. Lakowicz, "Fabrication and characterization of planar plasmonic substrates with high fluorescence enhancement," *J. Phys. Chem. C*, vol. 114, no. 49, pp. 21142–21149, Dec. 2010.

[30] E. Dulkeith *et al.*, "Fluorescence quenching of dye molecules near gold nanoparticles: Radiative and nonradiative effects," *Phys. Rev. Lett.*, vol. 89, no. 20, Oct. 2002, Art. no. 203002.

[31] E. Dulkeith, M. Ringler, T. A. Klar, J. Feldmann, A. M. Javier, and W. J. Parak, "Gold nanoparticles quench fluorescence by phase induced radiative rate suppression," *Nano Lett.*, vol. 5, no. 4, pp. 585–589, Apr. 2005.

[32] L. M. Liz-Marzán, "Nanometals," *Mater. Today*, vol. 7, pp. 26–31, 2004.

[33] C. W. Hsu *et al.*, "Transparent displays enabled by resonant nanoparticle scattering," *Nature Commun.*, vol. 5, no. 1, p. 3152, May 2014.

[34] S. Agnihotri, S. Mukherji, and S. Mukherji, "Size-controlled silver nanoparticles synthesized over the range 5–100 nm using the same protocol and their antibacterial efficacy," *RSC Adv.*, vol. 4, no. 8, pp. 3974–3983, 2014.

[35] J. A. Howarter and J. P. Youngblood, "Optimization of silica silanization by 3-aminopropyltriethoxysilane," *Langmuir*, vol. 22, pp. 11142–11147, 2006.

[36] E. T. Vandenberg *et al.*, "Structure of 3-aminopropyl triethoxy silane on silicon oxide," *J. Colloid Interface Sci.*, vol. 147, no. 1, pp. 103–118, Nov. 1991.

[37] K. Yuan, S.-J. Gu, Z.-F. Li, and X.-N. Shi, "WITHDRAWN: Preparation of poly(N-isopropylacrylamide) films on a modified silicon substrate via surface initiated redox polymerization," *Mater. Lett.*, vol. 4, pp. 1736–1740, Sep. 2006.

[38] J. Kim, P. Seidler, L. S. Wan, and C. Fill, "Formation, structure, and reactivity of amino-terminated organic films on silicon substrates," *J. Colloid Interface Sci.*, vol. 329, no. 1, pp. 114–119, Jan. 2009.

[39] H. P. Erickson, "Size and shape of protein molecules at the nanometer level determined by sedimentation, gel filtration, and electron microscopy," *Biol. Procedures Online*, vol. 11, no. 1, pp. 32–51, Dec. 2009.

[40] E. Droz, M. Taborelli, P. Descouts, and T. N. Wells, "Influence of surface and protein modification on immunoglobulin G adsorption observed by scanning force microscopy," *Biophys. J.*, vol. 67, no. 3, pp. 1316–1323, Sep. 1994.

[41] Y. Chen, J. Cai, Q. Xu, and Z. W. Chen, "Atomic force bioanalytics of polymerization and aggregation of phycoerythrin-conjugated immunoglobulin G molecules," *Mol. Immunol.*, vol. 41, pp. 1247–1252, 2004.

[42] E. W. Silverton, M. A. Navia, and D. R. Davies, "Three-dimensional structure of an intact human immunoglobulin," *Proc. Nat. Acad. Sci. USA*, vol. 74, pp. 5140–5144, 1977.

[43] Y. H. Tan, M. Liu, B. Nolting, J. G. Go, J. Gervay-Hague, and G.-Y. Liu, "A nanoengineering approach for investigation and regulation of protein immobilization," *ACS Nano*, vol. 2, no. 11, pp. 2374–2384, Nov. 2008.

[44] K. Aslan, J. R. Lakowicz, H. Szmacinski, and C. D. Geddes, "Metal-enhanced fluorescence solution-based sensing platform," *J. Fluorescence*, vol. 14, no. 6, pp. 677–679, Nov. 2004.

[45] Y. Zhang, A. Dragan, and C. D. Geddes, "Wavelength dependence of metal-enhanced fluorescence," *J. Phys. Chem. C*, vol. 113, no. 28, pp. 12095–12100, Jul. 2009.

[46] P. P. Pompa *et al.*, "Metal-enhanced fluorescence of colloidal nanocrystals with nanoscale control," *Nature Nanotechnol.*, vol. 1, p. 126, Sep. 2006.